

Preprint 01-2004

Ruhr University Bochum
Lehrstuhl für Technische Mechanik

**A 3D anisotropic elastoplastic-damage
model using discontinuous displacement
fields**

J. Mosler and O.T. Bruhns

This is a preprint of an article published in:
*International Journal for Numerical Methods in
Engineering*, Vol. 60, 923–948, (2004)

A 3D anisotropic elastoplastic-damage model using discontinuous displacement fields

J. Mosler

O.T. Bruhns

Lehrstuhl für Technische Mechanik

Ruhr University Bochum

Universitätsstr. 150, D-44780 Bochum, Germany

E-Mail: mosler@tm.bi.ruhr-uni-bochum.de

URL: www.tm.bi.ruhr-uni-bochum.de/mosler

Lehrstuhl für Technische Mechanik

Ruhr University Bochum

Universitätsstr. 150, D-44780 Bochum, Germany

E-Mail: bruhns@tm.bi.ruhr-uni-bochum.de

URL: www.tm.bi.ruhr-uni-bochum.de/bruhns

SUMMARY

This paper is concerned with the development of constitutive equations for finite element formulations based on discontinuous displacement fields. For this purpose, an elastoplastic continuum model (stress-strain relation) as well as an anisotropic damage model (stress-strain relation) are projected onto a surface leading to traction separation laws. The coupling of both continuum models and, subsequently, the derivation of the corresponding constitutive interface law are described in detail. For a simple calibration of the proposed model, the fracture energy resulting from the coupled elastoplastic-damage traction separation law is computed. By this, the softening evolution is linearly dependent on the fracture energy. The second part of the present paper deals with the numerical implementation. Based on a local and incompatible additive split of the displacement field into a continuous and a discontinuous part, the parameters specifying the jump of the displacement field are condensed out at the material level without employing the standard static condensation technique. To reduce locking effects, a rotating localization zone formulation is applied. The applicability and the performance of the proposed numerical implementation is investigated by means of a re-analysis of a two-dimensional L-shaped slab as well as by means of a three-dimensional ultimate load analysis of a steel anchor embedded in a concrete block.

1 INTRODUCTION

The prediction of the safety of engineering structures requires an adequate description of the structural response. Besides the ultimate load of the respective system, knowledge about the post-peak behavior is indispensable. Only by this means the type of collapse can be determined and taken into account.

Since the post-peak response is characterized by local (material point level) as well as global (structural response) strain softening, numerical analyses based on standard continuum approaches show the well known pathological mesh dependence [1]. Consequently, the requirement of enhanced continuum models to overcome these problems have been extensively addressed in the recent decade. In this respect, nonlocal models [2, 3], gradient-enhanced models [4, 5] and COSSERAT continua [6, 7] have to be mentioned. However, these models do not take the multiscale character of the underlying problem into account (in comparison to the dimensions of the structure, strain localization is restricted to narrow zones). Consequently, the resulting numerical effort is considerable.

As an alternative model, the Strong Discontinuity Approach (SDA) was proposed in [8–10]. In contrast to classical continuum models, the kinematic of the SDA is based on a discontinuous displacement field. These discontinuities are associated with the opening of cracks in brittle materials, LÜDERS bands or shear bands, respectively. Since the SDA accounts for the multi-scale character of the underlying problem, this approach is suitable for large scale computations [11, 12].

The coupling of the continuous and the discontinuous displacement field is provided by traction separation laws [8]. These constitutive interface laws can be developed by the projection of a stress strain law onto a material surface [8, 11, 13–15] or postulated independently [12, 16–18]. According to classical continuum mechanics, traction separation laws can be subdivided into plasticity based and damage based models. In [9, 19] an interface law was developed by projecting an isotropic associative plasticity model onto a surface. The extension to non-associated evolution equations was proposed in [15]. Damage-induced stiffness degradation has been considered in [8, 13, 20].

Real materials usually exhibit permanent plastic strains as well as the reduction of the stiffness. Consequently, the coupling of elastoplasticity with damage theory is necessary for a realistic modeling of the structural response. This coupling is accomplished by introducing an effective stress or by introducing damage-induced strains. This paper focuses on the second concept. More precisely, the elastoplastic anisotropic damage model suggested in [21] is applied for the development of a traction separation law. The resulting constitutive interface law is incorporated into a three-dimensional finite element formulation. The proposed implementation, similar to [11], is restricted to the material level and formally identical to the classical return mapping algorithm [22, 23]. As a consequence, the framework of computational plasticity can be applied.

The paper is organized as follows: Section 2 is concerned with a concise review of discontinuous displacement fields. In particular, the kinematic of the SDA is described in detail. The development of traction separation laws is addressed in Section 3. Based on a projection concept, a plasticity type (Subsection 3.1) and an anisotropic damage (Subsection 3.2) interface law are derived. Both models are coupled in Subsection 3.3 leading to an elastoplastic-damage traction separation law. The calibration of the resulting model is described in Subsection 3.4. Section 4 is concerned with the numerical implementation of the traction separation law. For this purpose, the numerically integrated constitutive equations are incorporated into a finite element formulation. The applicability of the proposed formulation is investigated in Section 5. In Subsection 5.1 an L-shaped slab is analyzed numerically. The robustness of the three-dimensional finite element model is demonstrated by means of the ultimate load analysis of an steel anchor embedded in a concrete block.

2 KINEMATICS: DISCONTINUITIES IN THE DISPLACEMENT FIELD

This section contains a concise summary of discontinuous displacement fields. Particularly, the kinematics of the Strong Discontinuity Approach (SDA) as proposed in [8–10, 24] and further elaborated in [11, 12, 15, 19, 20, 25–28] are described in detail. This section follows to a large extent [12].

A domain Ω of a body \mathcal{B} is considered to be separated into two parts Ω^- and Ω^+ by means of a localization surface $\partial_s\Omega$ (Figure 1). This surface is defined by its normal \boldsymbol{n} . Based on the assumption of a jump in the displacement field across this surface, an additive decomposition

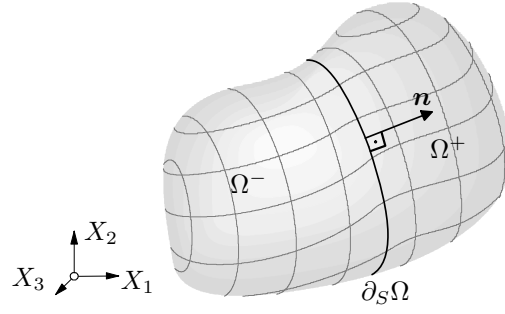


Figure 1: Body \mathcal{B} separated into two parts Ω^- and Ω^+ by a localization surface $\partial_s \Omega$

of the displacement field

$$\mathbf{u}(\mathbf{X}) = \bar{\mathbf{u}}(\mathbf{X}) + \hat{\mathbf{u}}(\mathbf{X}), \quad \forall \mathbf{X} \in \Omega, \quad (1)$$

into a continuous part $\bar{\mathbf{u}}(\mathbf{X}) \in \mathcal{C}^0(\mathbb{R}^3, \mathbb{R}^3)$ and a piecewise smooth function $\hat{\mathbf{u}}(\mathbf{X}) \in \mathcal{S}(\mathbb{R}^3, \mathbb{R}^3)$ (see Figure 2) is assumed [8–10, 24]. The additive split (1) holds for the SDA as well as for

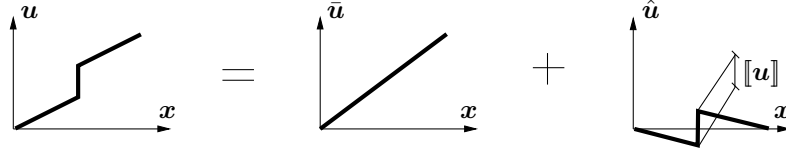


Figure 2: Additive decomposition of the displacement field into a continuous part $\bar{\mathbf{u}} \in \mathcal{C}^0(\mathbb{R}^3, \mathbb{R}^3)$ and a piecewise smooth function $\hat{\mathbf{u}} \in \mathcal{S}(\mathbb{R}^3, \mathbb{R}^3)$.

the Extended Finite Element Method (X-FEM) (see [29, 30]). The kinematics of the SDA are based on the additional restriction $\hat{\mathbf{u}} \in \mathcal{T}(\mathbb{R}^3, \mathbb{R}^3) \subset \mathcal{S}(\mathbb{R}^3, \mathbb{R}^3)$, with \mathcal{T} denoting the space of piecewise constant mappings. Consequently,

$$\lim_{\mathbf{X}^- \rightarrow \mathbf{A}} \frac{\partial \mathbf{u}}{\partial \mathbf{X}} = \lim_{\mathbf{X}^- \rightarrow \mathbf{A}} \frac{\partial \bar{\mathbf{u}}}{\partial \mathbf{X}} = \lim_{\mathbf{X}^+ \rightarrow \mathbf{A}} \frac{\partial \mathbf{u}}{\partial \mathbf{X}} \quad \forall \mathbf{A} \in \partial_s \Omega, \quad (2)$$

with $\mathbf{X}^- \in \Omega^-$ and $\mathbf{X}^+ \in \Omega^+$. Since the linearized strains $\boldsymbol{\varepsilon}$ are defined as $\boldsymbol{\varepsilon} = \nabla^{\text{sym}} \mathbf{u} := (\partial \mathbf{u} / \partial \mathbf{X})^{\text{sym}}$, the SDA is characterized by the restriction

$$\lim_{\mathbf{X}^- \rightarrow \mathbf{A}} \boldsymbol{\varepsilon}(\mathbf{X}^-) = \lim_{\mathbf{X}^+ \rightarrow \mathbf{A}} \boldsymbol{\varepsilon}(\mathbf{X}^+) \quad \forall \mathbf{A} \in \partial_s \Omega. \quad (3)$$

Hence, the strains in Ω^- and Ω^+ are not independent from each other. One discontinuous displacement field, fulfilling the restriction (3) has been proposed in [8, 9]

$$\mathbf{u} = \bar{\mathbf{u}} + [[\mathbf{u}]] H_s. \quad (4)$$

In Equation (4) $[[\mathbf{u}]]$ represents the displacement discontinuity defined as

$$[[\mathbf{u}]](\mathbf{A}) := \lim_{\mathbf{X}^+ \rightarrow \mathbf{A}} \mathbf{u}(\mathbf{X}^+) - \lim_{\mathbf{X}^- \rightarrow \mathbf{A}} \mathbf{u}(\mathbf{X}^-), \quad \text{with } \mathbf{A} \in \partial_s \Omega \quad (5)$$

and $H_s(\mathbf{X})$ denotes the HEAVISIDE function

$$\mathcal{T}(\mathbb{R}^3, \mathbb{R}) \ni H_s : \mathbb{R}^3 \rightarrow \mathbb{R} \\ \mathbf{X} \mapsto \begin{cases} 1 & \text{if } \mathbf{X} \in \Omega^+ \\ 0 & \text{if } \mathbf{X} \in \Omega^- \cup \partial_s \Omega. \end{cases} \quad (6)$$

From computing the gradient of Equation (4), using the derivative of the HEAVISIDE function $\nabla H_s = \mathbf{n} \delta_s$ [31], the linearized strain tensor is obtained as (see e.g. [13] for more details)

$$\boldsymbol{\varepsilon}(\mathbf{u}) = \nabla^{\text{sym}} \mathbf{u} = \nabla^{\text{sym}} \bar{\mathbf{u}} + \underbrace{([\mathbf{u}] \otimes \mathbf{n})^{\text{sym}}}_{\boldsymbol{\varepsilon}_\delta} \delta_s, \quad \|\mathbf{n}\|_2 = 1. \quad (7)$$

In Equation (7) the DIRAC-delta distribution δ_s has been introduced and it has been assumed that $\nabla [\mathbf{u}] = \mathbf{0}$. This assumption is motivated by the finite element implementation of the model, which is characterized by a constant direction and amplitude of the displacement jump with respect to the spatial coordinates within the domain Ω . For further details we refer to [11, 12, 32]. The modified strain tensor (7) contains, in addition to the gradient of the smooth part of the displacement field, the singular distribution $\boldsymbol{\varepsilon}_\delta \delta_s$. To simplify the following derivations, the rate of the displacement jump is represented by

$$[\dot{\mathbf{u}}] = \dot{\zeta} \mathbf{m}, \quad \|\mathbf{m}\|_2 = 1, \quad (8)$$

with the vector \mathbf{m} defining the direction of the jump, and ζ denoting the amplitude of the jump, respectively. Note, that Equation (8) does not imply $[\mathbf{u}] = \zeta \mathbf{m}$. Only for the special case $\dot{\mathbf{m}} = \mathbf{0}$ the identity $[\mathbf{u}] = \zeta \mathbf{m}$ holds. This assumption is very restrictive and consequently, it is not enforced in the present paper.

From the postulate $\nabla [\mathbf{u}] = \mathbf{0}$ follows that the additive decomposition (7) holds only in a local sense. Consequently, the singular strains $\boldsymbol{\varepsilon}_\delta \delta_s$ are not in general the symmetric gradient of a discontinuous displacement field. The local decomposition (7) is similar to the additive split $\boldsymbol{\varepsilon} = \boldsymbol{\varepsilon}^e + \boldsymbol{\varepsilon}^p$ used in standard plasticity models. Since Equation (7) has to be enforced locally (material point level), a rotating localization zone can be modeled. Of course, if macro-defects such as fully open cracks are considered, a rotating formulation would indeed be unphysical. However, the constitutive equations described in Section 3 are also applied to the modeling of micro-defects such as micro-cracks. These micro-cracks in fact do not rotate, but are closing, while additional micro-cracks start opening. In this respect, the rotating formulation, which fully captures this phenomenon, makes sense (see [11, 12]).

The vectors \mathbf{n} and \mathbf{m} representing the normal vector of the localization zone $\partial_s \Omega$ and the direction of the displacement jump, respectively, are computed from a bifurcation analysis, characterized by the localization condition

$$\mathbf{Q}^{\text{perf}} \cdot \mathbf{m} = \mathbf{0}, \quad (9)$$

with the acoustic tensor \mathbf{Q}^{perf} defined as (see [8, 33])

$$\mathbf{Q}^{\text{perf}} = \mathbf{n} \cdot \mathbb{C}_T^{\text{perf}} \cdot \mathbf{n}. \quad (10)$$

$\mathbb{C}_T^{\text{perf}}$ is the perfect plastic tangent operator. Though Equation (9) is formally identical to the classical localization condition (HADAMARD [34]), the derivations of both equations differ.

3 DEVELOPMENT OF TRACTION SEPARATION LAWS

This section is concerned with the development of traction separation laws. These laws connect the jump vector $[\mathbf{u}]$ with the traction vector \mathbf{t} representing the conjugate variable. The constitutive laws are derived by means of a projection of a stress-strain law onto the localization surface $\partial_s \Omega$.

The kinematics presented in Section 2 are based on two independent strain fields: $\nabla^{\text{sym}} \bar{\mathbf{u}}$ and $\varepsilon_\delta \delta_s$. The coupling between both tensors is provided by the compatibility condition

$$\boldsymbol{\sigma}^+ \cdot \mathbf{n} = \mathbf{t}^+ \equiv \mathbf{t}_s := [\boldsymbol{\sigma} \cdot \mathbf{n}]|_{\partial_s \Omega} \quad (11)$$

in terms of the traction vector \mathbf{t} acting on $\partial_s \Omega$. Note, that Equation (11) is not equivalent to the CAUCHY-lemma

$$[[\mathbf{t}]] = \mathbf{t}^+ - \mathbf{t}^- = \mathbf{0}. \quad (12)$$

While Equation (12) follows from the fundamental method of sections introduced by EULER, Equation (11) results from the principle of virtual work for continua with an internal surface $\partial_s \Omega$ and test functions $\boldsymbol{\eta}$ (virtual displacements) of the format

$$\boldsymbol{\eta} \in \mathcal{V} \subset \mathcal{S}(\mathbb{R}^3, \mathbb{R}^3), \quad (13)$$

with

$$\mathcal{V} := \{ \boldsymbol{\eta} = \boldsymbol{\eta}_0 + [[\boldsymbol{\eta}]] H_s \mid \boldsymbol{\eta}|_{\partial \Omega_u} = \mathbf{0}, \boldsymbol{\eta}_0 \in \mathcal{C}^\infty(\mathbb{R}^3, \mathbb{R}^3), [[\boldsymbol{\eta}]] \in \mathcal{C}^\infty(\partial_s \Omega, \mathbb{R}^3) \text{ arbitrary} \}. \quad (14)$$

In definition (14) $\partial \Omega_u$ denotes the DIRICHLET boundary. For further details we refer to [9] (see also [35]). While on the left hand side of Equation (11) the stresses follow from a standard continuum model, a constitutive law for the right hand side is required. Since the singular strains $\varepsilon_\delta \delta_s$ depend on the jump vector $[[\mathbf{u}]]$, a traction separation law has to be developed.

Remark 1: Condition $[[\mathbf{t}]](\mathbf{A}) = \lim_{\mathbf{X}^+ \rightarrow \mathbf{A}} \mathbf{t}(\mathbf{X}^+) - \lim_{\mathbf{X}^- \rightarrow \mathbf{A}} \mathbf{t}(\mathbf{X}^-) = \mathbf{0}$, $\forall \mathbf{A} \in \partial_s \Omega$ is fulfilled if and only if the left hand limit of \mathbf{t} at the point \mathbf{A} is identical to the right hand limit. However, condition $[[\mathbf{t}]] = \mathbf{0}$ does not imply anything about the value of \mathbf{t} at the point \mathbf{A} itself. Consequently, the mapping \mathbf{t} needs not to be continuous. Only if additionally $\lim_{\mathbf{X}^+ \rightarrow \mathbf{A}} \mathbf{t}(\mathbf{X}^+) = \mathbf{t}_s(\mathbf{A})$ is postulated $\mathbf{t} \in \mathcal{C}^0$.

One possible method to develop a traction separation law has been proposed by SIMO, OLIVER & ARMERO [8]. This concept is based on a projection of a standard continuum model onto a surface. Assuming a plasticity or damage based model, the homogeneously distributed dissipative mechanism is concentrated onto the singular surface $\partial_s \Omega$.

3.1 Plasticity theory

In this subsection, the concept of discontinuous displacement fields is incorporated into the governing equations of classical non-associated plasticity theory. It follows to a large extent previous formulations, as e.g. [8, 13, 19].

Without referring to any particular model of plasticity, the space of admissible stresses

$$\mathbb{E}\boldsymbol{\sigma} := \{ (\boldsymbol{\sigma}, \mathbf{q}) \in \mathbb{S} \times \mathbb{R}^n \mid \phi(\boldsymbol{\sigma}, \mathbf{q}) \leq 0 \} \quad (15)$$

is introduced. The convex set $\mathbb{E}\boldsymbol{\sigma}$ is defined by means of a yield function $\phi(\boldsymbol{\sigma}, \mathbf{q})$ in terms of the stress tensor $\boldsymbol{\sigma}$ lying in the space \mathbb{S} of symmetric rank two tensors and a vector of stress-like hardening/softening parameters \mathbf{q} . The model is constituted by the additive decomposition of the strains $\boldsymbol{\varepsilon}$ into an elastic part $\boldsymbol{\varepsilon}^e$ and a plastic part $\boldsymbol{\varepsilon}^p$, respectively, the definition of the stress rate, the evolution of the plastic strains and the internal variables $\boldsymbol{\alpha}$ conjugate to \mathbf{q} in the form

$$\begin{aligned} \dot{\boldsymbol{\varepsilon}}^e &= \dot{\boldsymbol{\varepsilon}} - \dot{\boldsymbol{\varepsilon}}^p \\ \dot{\boldsymbol{\sigma}} &= \mathbb{C} : \dot{\boldsymbol{\varepsilon}}^e, \quad \mathbb{C} = \partial_{\boldsymbol{\varepsilon}^e \otimes \boldsymbol{\varepsilon}^e} \Psi(\boldsymbol{\varepsilon}^e) \\ \dot{\boldsymbol{\varepsilon}}^p &= \lambda \frac{\partial g(\boldsymbol{\sigma}, \mathbf{q})}{\partial \boldsymbol{\sigma}}, \\ \dot{\boldsymbol{\alpha}} &= \lambda \frac{\partial h(\boldsymbol{\sigma}, \mathbf{q})}{\partial \mathbf{q}}. \end{aligned} \quad (16)$$

\mathbb{C} is the elastic 4th-order constitutive tensor, Ψ represents the free energy, $g(\boldsymbol{\sigma}, \mathbf{q})$ and $h(\boldsymbol{\sigma}, \mathbf{q})$ denote potential functions and λ is the plastic multiplier. For the special choice $h = \phi$ and $g = \phi$, the associated format is recovered. The model is completed by the KUHN-TUCKER conditions $\lambda \geq 0$, $\phi \leq 0$, $\lambda \phi = 0$. From the regular distribution of the stress tensor follows that the plastic multiplier λ

$$\lambda = \bar{\lambda} + \lambda_\delta \delta_s \quad (17)$$

must consist of a singular part $\lambda_\delta \delta_s$ in addition to a regular part $\bar{\lambda}$ [8]. The regular part $\bar{\lambda}$ is associated with a homogeneous deformation, while $\lambda_\delta \delta_s$ represents a localized deformation pattern. Since the development of a traction separation law, which is connected with a highly localized deformation, is the goal of this subsection, $\bar{\lambda} = 0$ is assumed. Consequently, plastic deformations are restricted to the surface $\partial_s \Omega$, while in Ω^\pm

$$\dot{\boldsymbol{\varepsilon}}^P = \mathbf{0}. \quad (18)$$

From Equations (7), (16), (17) and (18) together with the requirement of a regularly distributed traction vector follows, that the plastic strains $\boldsymbol{\varepsilon}^P$ are related to the singular strains

$$\dot{\boldsymbol{\varepsilon}}^P = ([\dot{\mathbf{u}}] \otimes \mathbf{n})^{\text{sym}} \delta_s = \lambda_\delta \frac{\partial g(\boldsymbol{\sigma}, \mathbf{q})}{\partial \boldsymbol{\sigma}} \delta_s. \quad (19)$$

Inserting Equation (19) into the consistency condition $\dot{\phi} = 0$, the linear relationship

$$\lambda_\delta = \zeta \frac{\partial \boldsymbol{\sigma} \phi : \mathbb{C} : (\mathbf{m} \otimes \mathbf{n})^{\text{sym}}}{\partial \boldsymbol{\sigma} \phi : \mathbb{C} : \partial \boldsymbol{\sigma} g} \quad (20)$$

between the singular plastic multiplier λ_δ and the amplitude of the displacement jump ζ is obtained. For further details we refer to [12, 13].

Alternatively to Equation (16)₄, the evolution of the strain-like internal variable $\boldsymbol{\alpha}$ is obtained as

$$\dot{\boldsymbol{\alpha}} = \frac{\partial \boldsymbol{\alpha}}{\partial \mathbf{q}} \cdot \dot{\mathbf{q}} =: \mathbf{H}^{-1} \cdot \dot{\mathbf{q}}. \quad (21)$$

According to the dimensions of $\boldsymbol{\alpha}$ and \mathbf{q} , the simple contraction in Equation (21) is referred to the \mathbb{R}^n . Since the yield function ϕ represents an equivalent stress and consequently, ϕ must be a regular distribution, the stress like internal variable \mathbf{q} must remain regularly distributed. In this respect, the plastic modulus \mathbf{H} has to be interpreted as a singular distribution (see e.g. [8]) resulting in

$$\mathbf{H}^{-1} = \bar{\mathbf{H}}^{-1} \delta_s \quad \Rightarrow \quad \dot{\mathbf{q}} = \lambda_\delta \bar{\mathbf{H}} \cdot \partial \mathbf{q} h. \quad (22)$$

Rewriting the consistency condition $\dot{\phi} = 0$ into the format

$$\partial \mathbf{q} \phi \cdot \dot{\mathbf{q}} = -\partial \boldsymbol{\sigma} \phi : \dot{\boldsymbol{\sigma}}, \quad (23)$$

together with Equation (22), results in the traction separation law

$$\boxed{\zeta = -\frac{1}{\partial \mathbf{q} \phi \cdot \bar{\mathbf{H}} \cdot \partial \mathbf{q} h} \frac{\partial \boldsymbol{\sigma} \phi : \mathbb{C} : \partial \boldsymbol{\sigma} g}{\partial \boldsymbol{\sigma} \phi : \mathbb{C} : (\mathbf{m} \otimes \mathbf{n})} \partial \boldsymbol{\sigma} \phi : \dot{\boldsymbol{\sigma}}} \quad (24)$$

connecting the amplitude of the displacement jump ζ with the stress tensor $\boldsymbol{\sigma}$.

The numerical examples contained in Section 5 are based on the RANKINE yield function. This yield function falls into the more general class of yield functions defined by

$$\phi(\boldsymbol{\sigma}, \boldsymbol{\alpha}) = (\mathbf{m} \otimes \mathbf{n}) : \boldsymbol{\sigma} - q(\boldsymbol{\alpha}). \quad (25)$$

Assuming associative evolution equations and inserting Equation (25) into Equation (20) leads to

$$\lambda_\delta = \dot{\zeta}. \quad (26)$$

and the traction separation law degenerates to

$$\boxed{\dot{\zeta} = -\frac{1}{H} (\mathbf{m} \otimes \mathbf{n}) : \dot{\boldsymbol{\sigma}}}. \quad (27)$$

From Equation (26) the local structure of the displacement field becomes obvious. Alternatively to the rate form (27), the integrated format

$$\phi(\boldsymbol{\sigma}, \alpha) = (\mathbf{m} \otimes \mathbf{n}) : \boldsymbol{\sigma} - q(\zeta) \quad (28)$$

can be applied. Equation (28) is formally equivalent to a yield function. However, its physical interpretation differs. Equation (28) represents a traction separation law connecting the component $\mathbf{m} \cdot \mathbf{t}$ of the traction vector with the amplitude of the displacement discontinuity.

3.2 Damage theory

In this subsection a traction separation law is developed by means of the anisotropic damage model proposed by GOVINDJEE, KAY & SIMO [36]. The presented derivation differs from the model suggested in [20]. For a detailed comparison between both model, we refer to [12].

The considered anisotropic damage model is based on the free energy potential

$$\Psi(\boldsymbol{\varepsilon}, \mathbb{C}, \alpha) = \frac{1}{2} \boldsymbol{\varepsilon} : \mathbb{C} : \boldsymbol{\varepsilon} + \Psi_{\text{in}}(\alpha). \quad (29)$$

According to Equation (29), the 4th-order constitutive tensor \mathbb{C} and α represent the internal variables. Assuming a yield function of the format (25), the evolution equations are obtained from the postulate of maximum dissipation as

$$\dot{\alpha} = \lambda \quad \text{and} \quad \mathbb{D} = \lambda \frac{\partial \boldsymbol{\sigma} \phi \otimes \partial \boldsymbol{\sigma} \phi}{\partial \boldsymbol{\sigma} \phi : \boldsymbol{\sigma}}, \quad \text{with} \quad \mathbb{D} := \mathbb{C}^{-1}. \quad (30)$$

For an efficient numerical implementation of the model, the rate form of the stress tensor is rewritten into the format

$$\begin{aligned} \dot{\boldsymbol{\sigma}} &= \mathbb{C} : \dot{\boldsymbol{\varepsilon}} + \dot{\mathbb{C}} : \boldsymbol{\varepsilon} = \mathbb{C} : \dot{\boldsymbol{\varepsilon}} - \mathbb{C} : \mathbb{D} : \mathbb{C} : \boldsymbol{\varepsilon} \\ &= \mathbb{C} : \dot{\boldsymbol{\varepsilon}} - \mathbb{C} : \underbrace{\partial \boldsymbol{\sigma} \phi \lambda}_{=: \dot{\boldsymbol{\varepsilon}}^d}. \end{aligned} \quad (31)$$

Equation (31) is formally equivalent to the rate form of a standard plasticity models. Consequently, the framework of computational plasticity can be applied. For the projection of the continuum model onto the surface $\partial_s \Omega$, we assume

$$\mathbb{D} = \bar{\mathbb{D}} + \mathbb{D}_\delta \delta_s, \quad \text{with} \quad \bar{\mathbb{D}} = \mathbb{D}_0 = \text{const}. \quad (32)$$

Hence the damage-induced dissipation is restricted to $\partial_s \Omega$. Using the rate form of Equation (32) and the condition of a regular distribution of the traction vector yields

$$([\dot{\mathbf{u}}] \otimes \mathbf{n})^{\text{sym}} = (\mathbf{m} \otimes \mathbf{n})^{\text{sym}} \dot{\zeta} = \mathbb{D}_\delta : \boldsymbol{\sigma}. \quad (33)$$

According to Equation (31) and (7), Equation (33) connects the singular and the damage-induced strains. From the assumed symmetry of the compliance tensor $[\mathbb{D}]_{ijkl} = [\mathbb{D}]_{klij}$ (this symmetry follows directly from the existence of an energy potential Ψ), together with Equation (33) and (25), the evolution of \mathbb{D} is obtained as

$$\dot{\mathbb{D}}_\delta = \dot{\zeta} \frac{(\mathbf{m} \otimes \mathbf{n})^{\text{sym}} \otimes (\mathbf{m} \otimes \mathbf{n})^{\text{sym}}}{(\mathbf{m} \otimes \mathbf{n}) : \boldsymbol{\sigma}}, \quad \text{with} \quad \dot{\zeta} = \lambda_\delta. \quad (34)$$

Since the identity $\dot{\zeta} = \lambda_\delta$ holds, the consistency condition $\dot{\phi} = 0$ results in (compare with Subsection 3.1)

$$\boxed{\dot{\zeta} = -\frac{1}{H} (\mathbf{m} \otimes \mathbf{n}) : \dot{\boldsymbol{\sigma}}}. \quad (35)$$

Consequently, the traction separation law (28) is recovered again.

3.3 Elastoplastic-damage model

This section is concerned with the development of a traction separation law based on an elastoplastic, anisotropic damage model. More precisely, the plasticity model described in Subsection 3.1 is coupled with the anisotropic damage model explained in Subsection 3.2. For the continuum case, the model was suggested in [21].

The elastoplastic-damage model is defined by means of the energy potential

$$\Psi(\boldsymbol{\varepsilon}^e, \mathbb{C}, \alpha) = \frac{1}{2} \boldsymbol{\varepsilon}^e : \mathbb{C} : \boldsymbol{\varepsilon}^e + \Psi_{\text{in}}(\alpha) \quad (36)$$

and a yield function of the format (25). Based on the postulate of maximum dissipation, the evolution equations are obtained as

$$\dot{\boldsymbol{\varepsilon}}^p + \underbrace{\dot{\mathbb{D}} : \boldsymbol{\sigma}}_{=: \dot{\boldsymbol{\varepsilon}}^d} = \lambda \partial_{\boldsymbol{\sigma}} \phi \quad \text{and} \quad \dot{\alpha} = \lambda \partial_q \phi. \quad (37)$$

A unique split of the inelastic strains into plastic and damage-induced strains is achieved by a scalar coupling parameter $\beta \in [0, 1]$ (see [21]). Consequently, the inelastic strains are computed as

$$\dot{\boldsymbol{\varepsilon}}^p = (1 - \beta) \lambda \partial_{\boldsymbol{\sigma}} \phi, \quad \dot{\boldsymbol{\varepsilon}}^d = \mathbb{D} : \boldsymbol{\sigma} = \beta \lambda \partial_{\boldsymbol{\sigma}} \phi \quad (38)$$

and the evolution of the compliance tensor results in

$$\dot{\mathbb{D}} = \beta \lambda \frac{\partial_{\boldsymbol{\sigma}} \phi \otimes \partial_{\boldsymbol{\sigma}} \phi}{\partial_{\boldsymbol{\sigma}} \phi : \boldsymbol{\sigma}}, \quad (39)$$

respectively. For $\beta = 0$ the plasticity model described in Subsection 3.1 is recovered. $\beta = 1.0$ is associated with the anisotropic damage model explained in Subsection 3.2. For the development of the traction separation law, we assume again the projection condition $\lambda = \lambda_\delta \delta_s$ leading to

$$\begin{aligned} \dot{\boldsymbol{\varepsilon}}^p &= \dot{\boldsymbol{\varepsilon}}_\delta^p \delta_s \\ \dot{\boldsymbol{\varepsilon}}^d &= \dot{\boldsymbol{\varepsilon}}_\delta^d \delta_s \quad \Rightarrow \quad \dot{\mathbb{D}} = \dot{\mathbb{D}}_\delta \delta_s. \end{aligned} \quad (40)$$

Consequently, the dissipation is restricted to $\partial_s \Omega$. From the requirement of a vanishing singular part of the traction vector, together with the assumption $\lambda = \lambda_\delta \delta_s$, the coupling of the singular strains $\boldsymbol{\varepsilon}_\delta \delta_s$ and the inelastic strains is provided by

$$\dot{\boldsymbol{\varepsilon}}_\delta \delta_s = (\mathbf{m} \otimes \mathbf{n})^{\text{sym}} \dot{\zeta} \delta_s = \dot{\boldsymbol{\varepsilon}}^p + \dot{\boldsymbol{\varepsilon}}^d. \quad (41)$$

According to Equation (38), the inelastic strains are additively decomposed by means of the scalar coupling parameter β

$$\begin{aligned} \dot{\boldsymbol{\varepsilon}}^p &= (1 - \beta) (\mathbf{m} \otimes \mathbf{n})^{\text{sym}} \dot{\zeta} \delta_s & \text{and} & \quad \dot{\boldsymbol{\varepsilon}}^d = \mathbb{D} : \boldsymbol{\sigma}, \quad \mathbb{D} = \mathbb{D}_\delta \delta_s. \\ \dot{\boldsymbol{\varepsilon}}^d &= \beta (\mathbf{m} \otimes \mathbf{n})^{\text{sym}} \dot{\zeta} \delta_s \end{aligned} \quad (42)$$

Using Equation (42)₂ and the existence of an energy potential ($[\mathbb{C}]_{ijkl} = [\mathbb{C}]_{klij}$ and $[\mathbb{D}]_{ijkl} = [\mathbb{D}]_{klij}$, respectively) yields the evolution of the singular part of the compliance tensor

$$\dot{\mathbb{D}}_\delta = \beta \dot{\zeta} \frac{(\mathbf{m} \otimes \mathbf{n})^{\text{sym}} \otimes (\mathbf{m} \otimes \mathbf{n})^{\text{sym}}}{(\mathbf{m} \otimes \mathbf{n}) : \boldsymbol{\sigma}}. \quad (43)$$

Since the rates of the stresses can be rewritten into the format

$$\begin{aligned} \dot{\boldsymbol{\sigma}} &= \dot{\mathbb{C}} : \boldsymbol{\varepsilon}^e + \mathbb{C} : \dot{\boldsymbol{\varepsilon}} - \mathbb{C} : \dot{\boldsymbol{\varepsilon}}^p \\ &= -\mathbb{C} : \dot{\mathbb{D}} : \mathbb{C} : \boldsymbol{\varepsilon}^e + \mathbb{C} : \dot{\boldsymbol{\varepsilon}} - (1 - \beta)\lambda \mathbb{C} : \partial \boldsymbol{\sigma} \phi \\ &= -\mathbb{C} : \dot{\mathbb{D}} : \boldsymbol{\sigma} + \mathbb{C} : \dot{\boldsymbol{\varepsilon}} - (1 - \beta)\lambda \mathbb{C} : \partial \boldsymbol{\sigma} \phi \\ &= \mathbb{C} : \dot{\boldsymbol{\varepsilon}} - \mathbb{C} : \partial \boldsymbol{\sigma} \phi \lambda, \end{aligned} \quad (44)$$

formally identical to Equation (16)₁₋₃ and Equation (31), the traction separation law

$$\boxed{\dot{\zeta} = -\frac{1}{H} (\mathbf{m} \otimes \mathbf{n}) : \dot{\boldsymbol{\sigma}}} \quad (45)$$

is recovered again.

Remark 2: $\beta = 0.5$ does not mean that 50% of the inelastic strains correspond to plastic strains and 50% to damage-induced strains. According to [21], an exponential softening evolution $q(\alpha)$ results for $\beta = 0$ in an exponential stress strain relationship. However, for $\beta = 1.0$ a linear stress strain law is obtained. Consequently, the influence of β on the decomposition of the inelastic strains becomes nonlinear.

3.4 Fracture energy

In this subsection the fracture energy resulting from the described material models is computed. Since the coupled elastoplastic-damage model proposed in Subsection 3.3 contains the plasticity model (Subsection 3.1) as well as the damage model (Subsection 3.2), it is sufficient to derive the fracture energy for this model.

Assuming localized inelastic deformations, the energy potential (36) converts to ([8, 12])

$$\Psi(\mathbb{C}, \boldsymbol{\varepsilon}^e, \zeta) = \Psi_e(\mathbb{C}, \boldsymbol{\varepsilon}^e) + \delta_s \Psi_{\text{in}}(\zeta), \quad \text{with} \quad \mathbb{C} = \mathbb{D}^{-1} \quad \text{and} \quad \mathbb{D} = \mathbb{D}_\delta \delta_s. \quad (46)$$

For the computation of the fracture energy \mathcal{G}_f the dissipation

$$\mathcal{D} = \boldsymbol{\sigma} : \dot{\boldsymbol{\varepsilon}} - \dot{\Psi} \geq 0 \quad (47)$$

has to be calculated. Consequently, the rate form of Equation (46) is required. From the kinematics (7), together with the decomposition (42) the rate of the elastic strains follows to

$$\dot{\boldsymbol{\varepsilon}}^e = \dot{\boldsymbol{\varepsilon}} + \dot{\boldsymbol{\varepsilon}}_\delta \delta_s - \dot{\boldsymbol{\varepsilon}}^p = \dot{\boldsymbol{\varepsilon}} + \beta (\mathbf{m} \otimes \mathbf{n})^{\text{sym}} \dot{\zeta} \delta_s \quad (48)$$

and the rate of the free energy results in

$$\begin{aligned} \dot{\Psi} &= \partial_{\boldsymbol{\varepsilon}^e} \Psi_e : \dot{\boldsymbol{\varepsilon}}^e + \partial_{\mathbb{C}} \Psi_e :: \dot{\mathbb{C}} + \partial_{\zeta} \Psi_{\text{in}} \dot{\zeta} \delta_s \\ &= \boldsymbol{\sigma} : \dot{\boldsymbol{\varepsilon}}^e - \frac{1}{2} \boldsymbol{\sigma} : \dot{\mathbb{D}}_\delta : \boldsymbol{\sigma} \delta_s + \partial_{\zeta} \Psi_{\text{in}} \dot{\zeta} \delta_s. \end{aligned} \quad (49)$$

Using the identity

$$\boldsymbol{\sigma} : \mathbb{D}_\delta : \boldsymbol{\sigma} = \beta \boldsymbol{\sigma} : (\mathbf{m} \otimes \mathbf{n}) \dot{\zeta} \quad (50)$$

the dissipation is obtained as

$$\mathcal{D} = \boldsymbol{\sigma} : \dot{\boldsymbol{\varepsilon}}_\delta \delta_s - \beta \boldsymbol{\sigma} : (\mathbf{m} \otimes \mathbf{n}) \dot{\zeta} \delta_s + \frac{1}{2} \beta \boldsymbol{\sigma} : (\mathbf{m} \otimes \mathbf{n}) \dot{\zeta} \delta_s - \partial_\zeta \Psi_{\text{in}} \dot{\zeta} \delta_s \geq 0. \quad (51)$$

For further details we refer to [12]. Introducing the notation $\mathcal{D}_\Omega := \int_\Omega \mathcal{D} \, dV$, together with the identity $\int_\Omega f \delta_s \, dV = \int_{\partial_s \Omega} f \, d\Gamma$ (see [31, 37, 38]), the global dissipation is computed as

$$\mathcal{D}_\Omega = \int_{\partial_s \Omega} \left[\left(1 - \frac{\beta}{2}\right) \mathbf{t} : [\dot{\mathbf{u}}] + q \dot{\zeta} \right] \, d\Gamma \geq 0, \quad (52)$$

with

$$q := -\partial_\zeta \Psi_{\text{in}}. \quad (53)$$

In contrast to classical continuum mechanics, Equation (52) represents a surface integral. From Equation (52) the global external stress power \mathcal{P}_Ω is obtained as

$$\mathcal{P}_\Omega = \mathcal{D}_\Omega + \int_\Omega \dot{\Psi} \, dV. \quad (54)$$

Integration of Equation (54) over the pseudo time t up to the formation of a macro crack ($t = t_u$) yields the corresponding energy

$$E = \int_{t=0}^{t_u} \mathcal{P}_\Omega \, dt. \quad (55)$$

Since a hyperelastic material is considered ($\int_{t=0}^{t_u} \dot{\Psi} \, dt = \int_{t=0}^{t_u} \dot{\Psi}_{\text{in}} \delta_s \, dt$) Equation (55) simplifies to

$$E = \int_{t=0}^{t_u} \int_{\partial_s \Omega} \left[\left(1 - \frac{\beta}{2}\right) \mathbf{t} : [\dot{\mathbf{u}}] \right] \, d\Gamma \, dt \geq 0. \quad (56)$$

The fracture energy \mathcal{G}_f is defined as

$$\mathcal{G}_f := \frac{E}{A_s}, \quad \text{with} \quad A_s := \int_{\partial_s \Omega} \, d\Gamma. \quad (57)$$

Assuming a constant integrand in Equation (56) with respect to \mathbf{X} , the fracture energy results in

$$\mathcal{G}_f = \left(1 - \frac{\beta}{2}\right) \int_{\zeta=0}^{\zeta_u} q(\zeta) \, d\zeta. \quad (58)$$

Equation (58) is independent of the size of the domain Ω . Consequently, finite element models based on traction separation laws are invariant with respect to the characteristic diameter of the discretization.

The numerical analyses of cracking in brittle structures presented in Section 5 are based on the softening evolution

$$q(\zeta) = f_{t_u} \frac{1}{\left(1 - \frac{\zeta}{\zeta_u}\right)^2}. \quad (59)$$

In Equation (59) f_{tu} denotes the uniaxial tensile strength and α_u represents a parameter describing the softening behavior. Applying Equation (58), the fracture energy is computed as

$$\mathcal{G}_f = \left(1 - \frac{\beta}{2}\right) f_{\text{tu}} \alpha_u. \quad (60)$$

Hence the softening variable α_u is obtained as

$$\alpha_u = \frac{\mathcal{G}_f}{\left(1 - \frac{\beta}{2}\right) f_{\text{tu}}}. \quad (61)$$

Remark 3: According to [21], the choice of $q(\zeta)$ is restricted by some thermodynamical principles. However, the evolution (61) is admissible.

4 NUMERICAL IMPLEMENTATION

This section contains the numerical implementation of the material model proposed in Subsection 3.3 by means of the finite element method. The algorithmic formulation is restricted to the material point level and follows to a large extent [11]. However, the presented finite element formulation is equivalent to the implementations proposed in [9, 19, 20, 24, 25, 27, 28] based on the enhanced assumed strain concept for constant strain elements. For more details concerning this equivalence, we refer to [12, 32, 39, 40].

4.1 Kinematics

For an efficient numerical formulation, the kinematics (4) and (7) are modified. However, the modified displacement field results in the same singular part $\varepsilon_\delta \delta_s$ of the strain tensor as obtained in Equation (7). Consequently, the traction separation laws proposed in Section 3 still hold.

According to [8, 9], the displacement field is assumed as

$$\mathbf{u} = \bar{\mathbf{u}} + [[\mathbf{u}]] M_s, \quad \text{with} \quad M_s(\mathbf{X}) = H_s(\mathbf{X}) - \varphi(\mathbf{X}), \quad \varphi \in \mathcal{C}^\infty(\mathbb{R}^3, \mathbb{R}). \quad (62)$$

Analogously to Section 2, the displacement field (62) can be decomposed into a continuous part

$$\bar{\mathbf{u}} + [[\mathbf{u}]] \varphi(\mathbf{X}) \in \mathcal{C}(\mathbb{R}^3, \mathbb{R}^3) \quad (63)$$

and a piecewise constant part

$$[[\mathbf{u}]] H_s(\mathbf{X}) \in \mathcal{T}(\mathbb{R}^3, \mathbb{R}^3). \quad (64)$$

The only difference between the kinematics (62) and Equation (7) is the smooth ramp function φ . The function $\varphi(\mathbf{X})$ allows to prescribe the boundary conditions in terms of $\bar{\mathbf{u}}$. Consequently, the discontinuous part of the displacement field has to vanish at all nodes (with coordinates \mathbf{X}_i^e) of the respective finite element. This restriction results in the condition

$$M_s(\mathbf{X}) = 0 \quad \forall \mathbf{X} = \mathbf{X}_i^e \quad i \in \{1, \dots, n_{\text{node}}\}. \quad (65)$$

Using the definition of the HEAVISIDE function (6),

$$\varphi(\mathbf{X}) = \begin{cases} 1 & \forall \mathbf{X} = \mathbf{X}_i^e \in \bar{\Omega}^{e+} \\ 0 & \forall \mathbf{X} = \mathbf{X}_i^e \in \bar{\Omega}^{e-} \end{cases} \quad i \in \{1, \dots, n_{\text{node}}\}. \quad (66)$$

is obtained. A suitable choice of the function φ complying with Equation (66) is represented by

$$\varphi(\boldsymbol{\xi}) = \sum_{i=1}^{n_{\Omega^+}} N_i(\boldsymbol{\xi}). \quad (67)$$

In Equation (67) N_i denotes the standard interpolation functions (see [11, 12]) and $\boldsymbol{\xi}$ represents the vector of natural coordinates. The shape of the approximated discontinuous displacement field resulting from bi-linear shape functions is shown in Figure 3. Since φ can be expressed

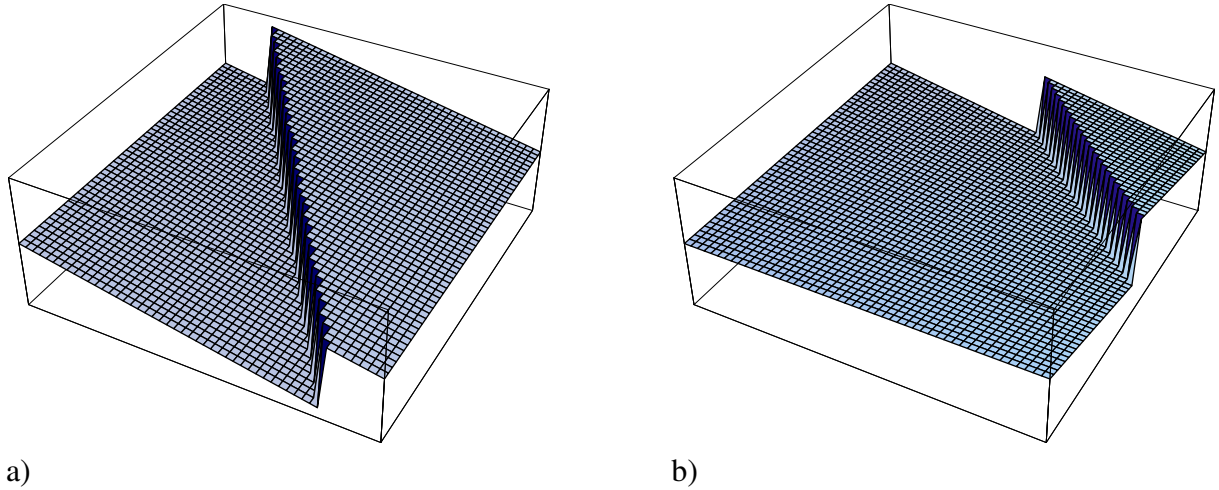


Figure 3: Two possible modes of the discontinuous shape function $M_s(\mathbf{X})$ using bi-linear functions φ . a) A localization surface is cutting two opposite edges of the finite element, b) a localization surface is cutting two adjacent edges of the finite element

as a sum of standard interpolation functions, the discontinuous displacement field is piecewise bi-linear. From computing the gradient of Equation (62), using Equation (67), the linearized strain tensor is obtained as (see [9, 39] for more details)

$$\boldsymbol{\varepsilon}(\mathbf{u}) = \nabla^{\text{sym}} \mathbf{u} = \nabla^{\text{sym}} \bar{\mathbf{u}} - \underbrace{([\mathbf{u}] \otimes \nabla \varphi)^{\text{sym}}}_{:= \tilde{\boldsymbol{\varepsilon}}} + \boldsymbol{\varepsilon}_\delta \delta_s. \quad (68)$$

Remark 4: The proposed numerical implementation is restricted to the material point level. For non-constant functions $\nabla \varphi$ the average value

$$\overline{\nabla \varphi} := \frac{1}{V^e} \int_{\Omega^e} \nabla \varphi \, dV, \quad \text{with} \quad V^e := \int_{\Omega^e} dV \quad (69)$$

is employed. For further details, we refer to [11, 12].

Remark 5: According to Equation (68), the enhanced strains $\tilde{\boldsymbol{\varepsilon}}$ depend on $\nabla \varphi$. Since the gradient of φ is computed via

$$\nabla \varphi = \sum_{i=1}^{n_{\Omega^+}} \frac{\partial N_i}{\partial \boldsymbol{\xi}} \cdot \underbrace{\frac{\partial \boldsymbol{\xi}}{\partial \mathbf{X}}}_{= \mathbf{J}^{-1}} \quad (70)$$

in terms of the JACOBI matrix \mathbf{J} , an internal length l_c is implicitly introduced into the finite element formulation [12, 40].

4.2 Re-formulation of the elastoplastic-damage model

As shown in Subsection 3.3, the singular strains $\epsilon_\delta \delta_s$ are equivalent to the sum of the plastic strains and the damage-induced strains (see Equation (41)). Equation (41) implies an additive decomposition of the amplitude of the displacement discontinuity of the format

$$\dot{\zeta} = \dot{\zeta}^p + \dot{\zeta}^d, \quad \text{with} \quad \begin{aligned} \dot{\zeta}^p &= (1 - \beta) \dot{\zeta} \\ \dot{\zeta}^d &= \beta \dot{\zeta} \end{aligned} \quad (71)$$

As a consequence, the regularly distributed strains $\tilde{\epsilon}$ are split into

$$\dot{\tilde{\epsilon}} = \dot{\tilde{\epsilon}}^p + \dot{\tilde{\epsilon}}^d, \quad \text{with} \quad \begin{aligned} \dot{\tilde{\epsilon}}^p &= (1 - \beta) \dot{\tilde{\epsilon}} \\ \dot{\tilde{\epsilon}}^d &= \beta \dot{\tilde{\epsilon}} \end{aligned} \quad (72)$$

From the equivalence of the stress rate (see Equation (44))

$$\begin{aligned} \dot{\sigma} &= \mathbb{C} : (\dot{\epsilon} - \partial \sigma \phi \lambda) \\ &= \mathbb{C} : (\nabla^{\text{sym}} \dot{\mathbf{u}} - \dot{\tilde{\epsilon}}) \end{aligned} \quad (73)$$

and the alternative format

$$\dot{\sigma} = \mathbb{C} : (\nabla^{\text{sym}} \dot{\mathbf{u}} - \dot{\tilde{\epsilon}}^p) + \dot{\mathbb{C}} : (\nabla^{\text{sym}} \bar{\mathbf{u}} - \tilde{\epsilon}^p), \quad (74)$$

the identity

$$\dot{\tilde{\epsilon}}^d = \dot{\mathbb{D}} : \sigma \quad (75)$$

follows. Introducing the second order tensor

$$\mathbf{G} := (\mathbf{m} \otimes \nabla \varphi)^{\text{sym}}, \quad (76)$$

which defines the direction of the regularly distributed enhanced strains $\tilde{\epsilon}$, and forming the scalar product of Equation (75) with the stress tensor yields the evolution of the regularly distributed compliance tensor

$$\begin{aligned} \sigma : \dot{\mathbb{D}} : \sigma &= \beta \dot{\zeta} \sigma : \mathbf{G} \\ &= \beta \dot{\zeta} \sigma : \mathbf{G} \frac{(\mathbf{m} \otimes \mathbf{n}) : \sigma}{(\mathbf{m} \otimes \mathbf{n}) : \sigma} \\ &= \beta \dot{\zeta} \sigma : \frac{\mathbf{G} \otimes (\mathbf{m} \otimes \mathbf{n})^{\text{sym}}}{(\mathbf{m} \otimes \mathbf{n}) : \sigma} : \sigma \\ &\Rightarrow \boxed{\dot{\mathbb{D}} = \beta \dot{\zeta} \frac{\mathbf{G} \otimes (\mathbf{m} \otimes \mathbf{n})^{\text{sym}}}{(\mathbf{m} \otimes \mathbf{n})^{\text{sym}} : \sigma}} \end{aligned} \quad (77)$$

Remark 6: The multiplication by $(\mathbf{m} \otimes \mathbf{n}) : \sigma / (\mathbf{m} \otimes \mathbf{n}) : \sigma$ used in Equation (77) follows from an analogy to the enhanced strains. The rates of the regularly and the singularly distributed enhanced strains are defined by

$$\begin{aligned} \dot{\tilde{\epsilon}} &= (\mathbf{m} \otimes \nabla \varphi)^{\text{sym}} \dot{\zeta} \\ \dot{\epsilon}_\delta \delta_s &= (\mathbf{m} \otimes \mathbf{n})^{\text{sym}} \dot{\zeta} \delta_s. \end{aligned} \quad (78)$$

According to Equation (78), the directions of these rates are defined by means of the tensor product of two first order tensors. The first vector of the tensor product \mathbf{m} coincides for both directions. By means of the applied multiplication used for the derivation of the compliance tensor, this analogy holds also for the regularly and singularly distributed compliance tensor (compare Equations (77) and (43)).

4.3 Integration of the constitutive equations

This subsection contains the numerical implementation of the constitutive equations. Following the algorithmic formulation proposed in [11], the localization surface $\partial_s \Omega$ may rotate. By this, locking phenomena are reduced [11]. Without applying a rotating formulation intersecting cracks have to be taken into account. Numerical methods based on a single fixed crack cannot model the difference between primary and secondary cracks (see [11]).

At the end of a time interval $[t_n, t_{n+1}]$, the updated state of stress (see Equation (74)) and of the softening parameter q , respectively, is

$$\begin{aligned}\boldsymbol{\sigma}_{n+1} &= \mathbb{C}_{n+1} : (\nabla^{\text{sym}} \bar{\mathbf{u}}_{n+1} - \tilde{\boldsymbol{\varepsilon}}_{n+1}^{\text{p}}), \\ q_{n+1} &= q_{n+1}(\zeta_{n+1}).\end{aligned}\quad (79)$$

With the definition of a trial state

$$\begin{aligned}\boldsymbol{\sigma}_{n+1}^{\text{tr}} &= \mathbb{C}_n : (\nabla^{\text{sym}} \bar{\mathbf{u}}_{n+1} - \tilde{\boldsymbol{\varepsilon}}_n^{\text{p}}) \\ q^{\text{tr}} &= q(\zeta_n)\end{aligned}\quad (80)$$

characterized by pure elastic deformations ($\dot{\zeta} = 0$), the trial loading condition is given as

$$\phi_{n+1}^{\text{tr}}(\boldsymbol{\sigma}_{n+1}^{\text{tr}}, q_{n+1}^{\text{tr}}) > 0. \quad (81)$$

Application of a backward EULER integration to the evolution of the regularly distributed strains and the evolution of the amplitude of the displacement discontinuity together with the failure criterion at t_{n+1} leads to

$$\begin{aligned}\tilde{\boldsymbol{\varepsilon}}_{n+1} &= \tilde{\boldsymbol{\varepsilon}}_n + \mathbf{G}_{n+1} \Delta \zeta_{n+1}, \\ \zeta_{n+1} &= \zeta_n + \Delta \zeta_{n+1}, \quad \text{with } \Delta(\bullet)_{n+1} := (\bullet)_{n+1} - (\bullet)_n, \\ \phi_{n+1} &= (\mathbf{m}_{n+1} \otimes \mathbf{n}_{n+1}) : \boldsymbol{\sigma}_{n+1} - q_{n+1} = 0\end{aligned}\quad (82)$$

Combining Equations (80)₁ and (82)₁, Equation (79)₁ can be reformulated into the format

$$\boldsymbol{\sigma}_{n+1} = \boldsymbol{\sigma}_{n+1}^{\text{tr}} - \mathbb{C}_n : \mathbf{G}_{n+1} \Delta \zeta_{n+1}. \quad (83)$$

Equation (83) is formally identical to standard computational plasticity. For $\beta = 0$ associated with a plasticity interface traction separation law, this equivalence has been shown in [11, 39].

Since the following numerical implementation of the proposed coupled elastoplastic-damage model is similar to the algorithmic formulation in [11, 12], only the resulting equations are presented. Using NEWTON's method based on a consistent linearization, the increment of the amplitude of the displacement jump during an iteration cycle is obtained in matrix notation as

$$d\Delta \zeta_{n+1} = \frac{\phi_{n+1} - \nabla \phi^T \mathbf{A} \mathbf{R}}{\nabla \phi^T \mathbf{A} \nabla M}. \quad (84)$$

In Equation (84) the definitions

$$\begin{aligned}\nabla \phi^T &:= [(\mathbf{m}_{n+1} \otimes \mathbf{n}_{n+1}); -1] \\ \nabla M^T &:= [\mathbf{G}_n; 1] \\ \mathbf{R}^T &:= \begin{bmatrix} \mathbf{R}^{\tilde{\boldsymbol{\varepsilon}}} \\ R^\zeta \end{bmatrix}, \quad \text{with } \begin{aligned} \mathbf{R}^{\tilde{\boldsymbol{\varepsilon}}} &:= -\tilde{\boldsymbol{\varepsilon}}_{n+1} + \tilde{\boldsymbol{\varepsilon}}_n + \mathbf{G}_{n+1} \Delta \zeta_{n+1} \\ R^\zeta &:= -\zeta_{n+1} + \zeta_n + \Delta \zeta_{n+1} \end{aligned} \\ \mathbf{A}^{-1} &:= \begin{bmatrix} \boldsymbol{\Xi}_{n+1}^{-1} & \mathbf{0} \\ 0 & D^{-1} \end{bmatrix}\end{aligned}\quad (85)$$

have been used. Ξ_{n+1} represents the algorithmic moduli

$$\Xi_{n+1}^{-1} = \mathbb{C}_n^{-1} + \mathbb{G}_{n+1}^{\text{sym}}, \quad \text{with} \quad \mathbb{G}_{n+1}^{\text{sym}} = \Delta\zeta_{n+1} \left(\nabla\varphi \otimes \frac{\partial \mathbf{m}_{n+1}}{\partial \boldsymbol{\sigma}_{n+1}} \right)^{\text{sym}} \quad \mathbb{G}_{ijkl}^T = \mathbb{G}_{jikl} \quad (86)$$

and D the slope of the softening evolution, respectively,

$$D = -\frac{\partial q}{\partial \zeta}. \quad (87)$$

The convergence of the NEWTON-iteration is checked according to the criterion

$$\max(\|\mathbf{R}\|_\infty, |\phi|) < \text{tol}. \quad (88)$$

The numerical analyses presented in Section 5 are based on $\text{tol} = 10^{-10}$. For a globally convergent behavior at an asymptotic quadratic rate, the algorithmic tangent tensor needs to be computed from the consistent linearization of the algorithm at t_{n+1} , where the residuals $\mathbf{R} = \mathbf{0}$. The algorithmic elastoplastic-damage tangent tensor is obtained as

$$\begin{aligned} \mathbb{C}^{\text{ep}} &= \frac{d\boldsymbol{\sigma}}{d\nabla^{\text{sym}}\bar{\mathbf{u}}} = \Xi - \frac{\{\mathbf{A} \nabla M \otimes \nabla \phi^T \mathbf{A}\}_{[11]}}{\nabla \phi^T \mathbf{A} \nabla M} \\ &= \Xi - \frac{\Xi : \mathbf{G} \otimes (\mathbf{m} \otimes \mathbf{n}) : \Xi}{(\mathbf{m} \otimes \mathbf{n}) : \Xi : \mathbf{G} - D}, \end{aligned} \quad (89)$$

where the abbreviation $[\bullet]_{[11]}$ for the submatrix 11 has been used. Although an associated flow is used, linearization results in a non-symmetric 4th-order tensor \mathbb{C}^{ep} . This results directly from the PETROV-GALERKIN discretization of the enhanced strains [11, 12, 40]. Based on the update values of $\boldsymbol{\sigma}$, \mathbf{m} and \mathbf{n} , the increment of the regularly distributed compliance tensor $\tilde{\mathbb{D}}$ is computed as

$$\Delta\tilde{\mathbb{D}} = \beta \Delta\zeta_{n+1} \frac{\mathbf{G}_{n+1} \otimes (\mathbf{m}_{n+1} \otimes \mathbf{n}_{n+1})^{\text{sym}}}{(\mathbf{m}_{n+1} \otimes \mathbf{n}_{n+1}) : \boldsymbol{\sigma}_{n+1}}. \quad (90)$$

The constitutive tensor \mathbb{C} follows from

$$\tilde{\mathbb{D}}_{n+1} = \mathbb{D}_0 + \sum_{i=0}^n \Delta\tilde{\mathbb{D}}_{i+1} \quad \Rightarrow \quad \mathbb{C}_{n+1} = \tilde{\mathbb{D}}_{n+1}^{-1}. \quad (91)$$

The necessary inversion of the compliance tensor can be determined directly or by means of the SHERWIN-MORRISON-WOODBURY theorem.

Remark 7: According to Equation (89), the condition

$$(\mathbf{m} \otimes \mathbf{n}) : \Xi : \mathbf{G} - D > 0 \quad (92)$$

has to be fulfilled. Otherwise a snap back in the stress strain relation occurs. In [41] a similar condition was derived for plasticity and damage based interface laws using constant strain triangular elements. However, the format (92) holds independently of the respective element type and the considered material [12].

Remark 8: For the linearization (86), $\partial\nabla\varphi/\partial\boldsymbol{\sigma} = \mathbf{0}$ has been assumed. Since $\varphi = \varphi(\mathcal{X}^+)$ with

$$\mathcal{X}^+ := \{\mathbf{X} \in \bar{\Omega}^+ \mid \exists! \mathbf{X}_i^e, 1 \leq i \leq n_{\text{node}}, \quad \mathbf{X} = \mathbf{X}_i^e\}, \quad (93)$$

$\nabla\varphi$ only depends on the set \mathcal{X}^+ . Consequently, if \mathcal{X}^+ does not change, the assumption $\partial\nabla\varphi/\partial\boldsymbol{\sigma} = \mathbf{0}$ holds. However, it is possible that \mathcal{X}^+ changes. In this case, the NEWTON iteration is repeated with the updated set \mathcal{X}^+ . If the mode $\nabla\varphi$ jumps again, the rotating localization formulation is replaced by a fixed localization formulation [12]. In the next global load step it is switched back to the rotating localization formulation.

4.4 Finite element formulation

For the derivation of the finite element formulation, the weak form of equilibrium is considered

$$\int_{\Omega^e} \nabla^{\text{sym}} \bar{\eta} : \boldsymbol{\sigma} \, dV = \int_{\Omega^e} \bar{\eta} \cdot \mathbf{f} \, dV + \int_{\Gamma_{\boldsymbol{\sigma}}^e} \bar{\eta} \cdot \mathbf{t}^* \, d\Gamma. \quad (94)$$

In Equation (94) $\bar{\eta}$ denotes a continuous testfunction, \mathbf{f} body forces and \mathbf{t}^* prescribed traction vectors acting on the NEUMANN boundary $\Gamma_{\boldsymbol{\sigma}}$. As explained in Section 2 and 3, the discontinuous part of the displacement field is restricted to the material point level. Consequently, $\bar{\mathbf{u}}$ represents the only global displacement field. According to GALERKIN-type approximations of the continuous displacement field the approximation of the fields $\bar{\mathbf{u}}$ and $\bar{\eta}$ are assumed as

$$\begin{aligned} \bar{\mathbf{u}} &\approx \sum_{i=1}^{n_{\text{node}}} N_i \bar{\mathbf{u}}_i^e & \nabla \bar{\mathbf{u}} &\approx \sum_{i=1}^{n_{\text{node}}} \bar{\mathbf{u}}_i^e \otimes \nabla N_i \\ \bar{\eta} &= \sum_{i=1}^{n_{\text{node}}} N_i \bar{\eta}_i^e & \nabla \bar{\eta} &= \sum_{i=1}^{n_{\text{node}}} \bar{\eta}_i^e \otimes \nabla N_i. \end{aligned} \quad (95)$$

Since the global solution strategy of the nonlinear Equation (94) is based on NEWTON's method, the linearization of Equation (94) has to be computed. Using Equation (89), this linearization results in

$$\int_{\Omega^e} \nabla^{\text{sym}} \bar{\eta} : \mathbb{C}^{\text{ep}} : \nabla^{\text{sym}} \Delta \bar{\mathbf{u}} \, dV = \int_{\Omega^e} \bar{\eta} \cdot \Delta \mathbf{f} \, dV + \int_{\Gamma_{\boldsymbol{\sigma}}^e} \bar{\eta} \cdot \Delta \mathbf{t}^* \, d\Gamma. \quad (96)$$

Equations (94)-(96) are formally identical to standard continuum models. Therefore, any computer code for plasticity models can directly be used as the framework for the implementation of the proposed elastoplastic-damage model.

5 NUMERICAL EXAMPLES

The applicability and performance of the proposed numerical implementation is investigated by means of a re-analysis of a two-dimensional L-shaped slab (Subsection 5.1) as well as by means of an ultimate load analysis of a steel anchor embedded in a concrete block (Subsection 5.2). For prognoses of mode-I fracture of brittle materials, the RANKINE yield function characterized by $\mathbf{n} = \mathbf{m}$ is adopted. Applying the rotating formulation described in Subsection 4.3, the vectors \mathbf{n} and \mathbf{m} coincide with the direction of the maximum principle stress.

5.1 L-shaped slab

This subsection is concerned with a re-analysis of an L-shape slab [42–44]. The geometry and material parameters of the problem are illustrated in Figure 4. According to Equation (59), a hyperbolic softening evolution is assumed. The displacement controlled analysis is performed by means of 642 bilinear 4 node plane stress elements. Loading was applied by prescribing vertical displacements at all nodes along the right edge of the slab. Convergence is checked according to the criterion

$$\frac{\|\mathbf{r}_i - \mathbf{r}_e\|_{\infty}}{\|\mathbf{r}_e\|_{\infty}} < \text{tol}, \quad (97)$$

where \mathbf{r}_i (\mathbf{r}_e) is the vector of internal (external) forces. For the numerical analyses of the L-shaped slab, tol is set to $\text{tol} = 10^{-8}$.

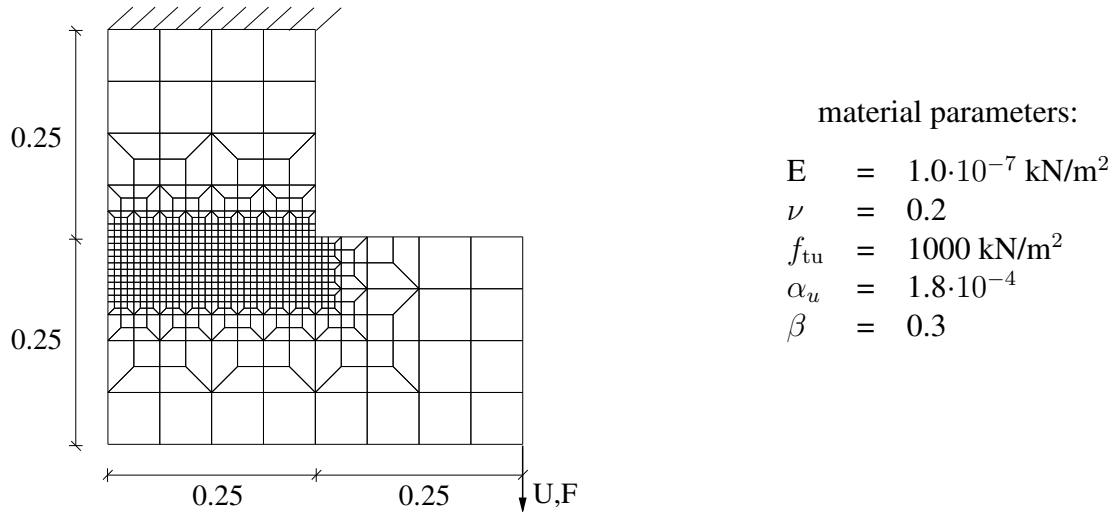


Figure 4: 2D finite element analysis of an L-shaped slab: Geometry (dimensions in [m]), discretization and material parameters (thickness of the slab=0.2 m)

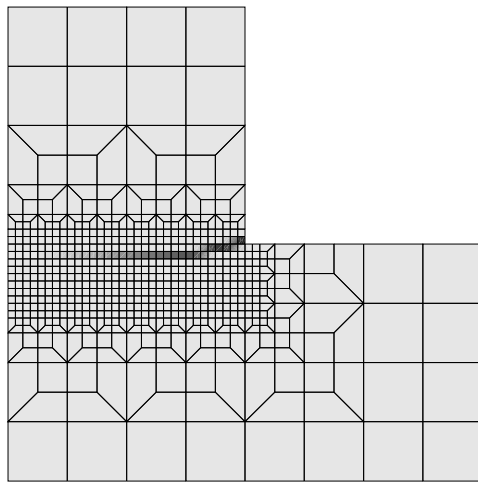
Figure 5b shows the load-displacement diagram obtained from the analysis. In the post-peak regime, four unloading and reloading cycles have been included. This diagram illustrates the capability of the model to capture fracture-induced stiffness degradation as well as permanent deformations after crack initiation. Damage accumulation, characterized by the internal variable α is illustrated in Figure 5a. A localized, slightly curved crack band is observed. It refers to the final state of the loading process. The computed results agree with the numerical analyses reported in [42–44].

5.2 Pull-out of a steel anchor embedded in a concrete block

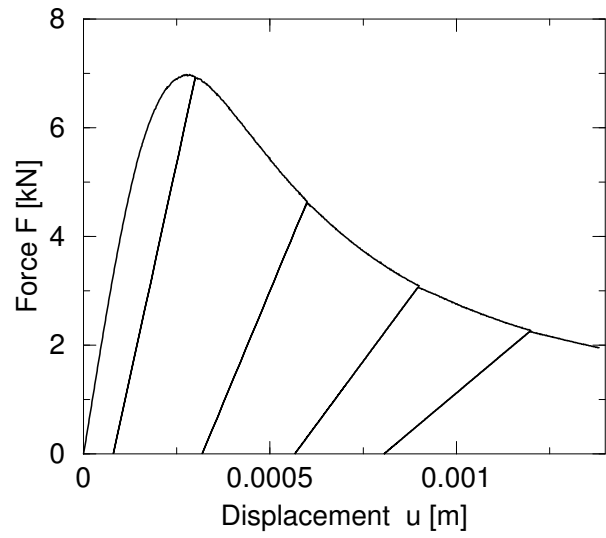
The three-dimensional finite element formulation proposed in Section 4 is employed for the numerical analysis of a steel anchor embedded within a block of concrete which is subjected to a tensile loading. This problem has been previously analyzed experimentally as well as numerically in [45]. The geometry and the material parameters of the concrete block (80 cm \times 40 cm \times 38 cm) and the steel anchor (diameter of the stud 4 cm, diameter of the steel truss 2 cm) together with the DIRICHLET and NEUMANN boundary conditions are illustrated in Figure 6. In the presented numerical analysis only tensile cracking is taken into account, although the experiments documented in [45] indicate a relatively strong influence of the compression strength on the maximum loading. According to Equation (59), a hyperbolic softening evolution is chosen. The material behavior of the steel anchor is approximated by HOOKE's law. Between the steel of the headed stud and the concrete block frictionless contact is assumed.

In Figure 7 the discretizations used for the analyses are illustrated. The coarse mesh consists of 820 tri-linear 8-noded elements and the fine mesh contains 2802 elements, respectively. The necessary CPU time of the computations is reduced by taking into account the symmetry of the geometry and the boundary conditions. Loading is applied by increasing the vertical displacement of the headed stud by steps of $\Delta u_1 = 2.156 \cdot 10^{-4}$ cm. According to Equation (97), convergence is checked by the maximum norm assuming $tol = 10^{-6}$.

The load-displacement diagrams of the numerical analyses are illustrated in Figure 8. Both discretizations predict an almost identical maximum loading. With a maximum loading of 115.7 kN (fine mesh) and 117.5 kN (coarse mesh), respectively, the relative difference follows to 1.6%. Consequently, only a minor influence of the chosen discretization on the peak load is

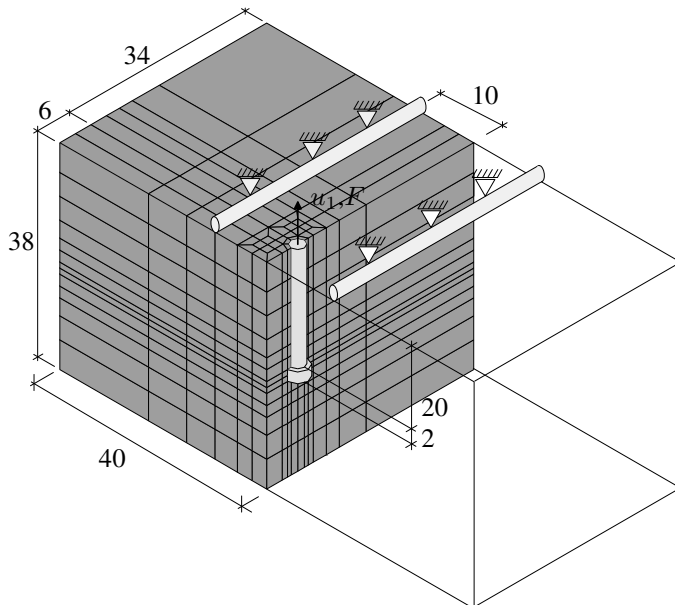


a)



b)

Figure 5: 2D finite element analysis of a L-shaped slab: a) Distribution of the internal variable ζ , b) load-displacement diagram.



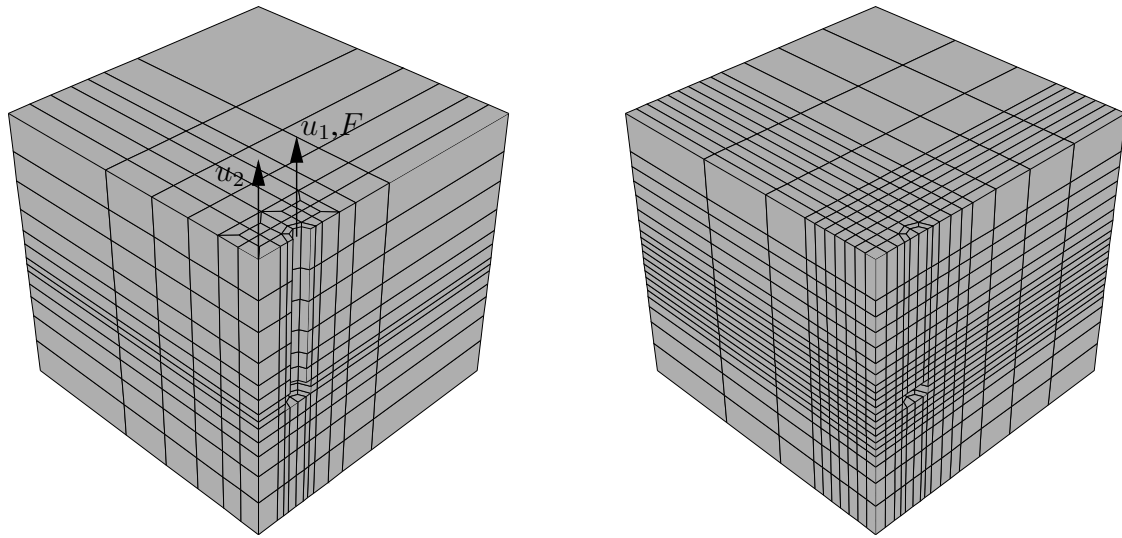
concrete:

$$\begin{aligned}
 E &= 3500 \quad [\text{KN}/\text{cm}^2] \\
 \nu &= 0.2 \\
 \mathcal{G}_f &= 7.5 \cdot 10^{-4} [\text{KN cm}/\text{cm}^2] \\
 f_{\text{tu}} &= 0.25 \quad [\text{KN}/\text{cm}^2] \\
 \beta &= 0.2
 \end{aligned}$$

steel:

$$\begin{aligned}
 E &= 21000 [\text{KN}/\text{cm}^2] \\
 \nu &= 0.3
 \end{aligned}$$

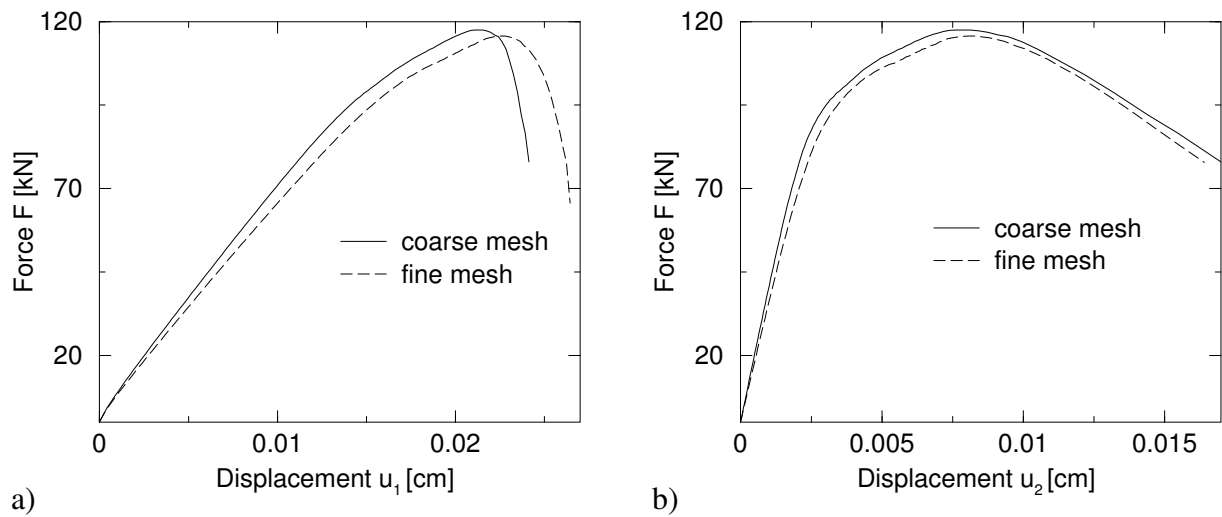
Figure 6: 3D finite element analysis of an anchor subjected to tensile loading: Dimensions (in [cm]) and material parameters.



a)

b)

Figure 7: 3D finite element analysis of an anchor subjected to tensile loading: Finite element discretizations a) coarse mesh (820 tri-linear elements), b) fine mesh (2802 tri-linear elements).



a)

b)

Figure 8: 3D finite element analysis of an anchor subjected to tensile loading: Load-displacement diagrams a) displacement u_1 , b) displacement u_2 (see Figure 7).

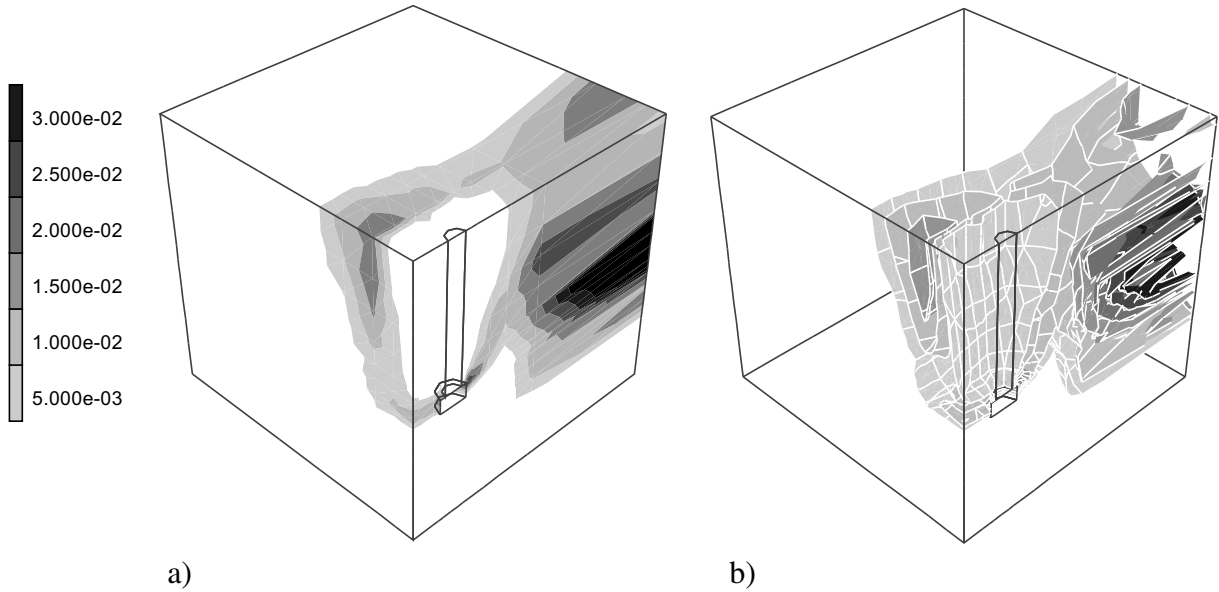


Figure 9: 3D finite element analysis of an anchor subjected to tensile loading (coarse mesh): Distribution of the internal variable α representing the crack-width at $u_1 = 2.37 \cdot 10^{-2}$ cm: a) Contours along the surfaces, b) iso-surfaces.

reflected in the diagrams. If the prescribed displacement u_1 is increased more than 0.021 cm, the structural response is characterized by softening. However, the differences of the post-peak behavior resulting from the analyses of the coarse and the fine mesh are marginal. The maximum loading obtained from numerical analyses of only half of the structure reported in [45] are ranging between 67 kN (for the compressive strength of concrete chosen as $f_{cu} = 20$ MPa) and 94 kN (for $f_{cu} = 40$ MPa). The respective experimental data are ranging between 69 kN and 75 kN [45]. Since failure in compression has not been considered in the present analysis, implying a compression strength $f_{cu} = \infty$, the difference of 115.7 kN-94 kN=21.7 kN (23%) seems to be reasonable.

Figures 9 and 10 illustrate the distribution of the internal variable α obtained from the coarse mesh and the fine mesh, respectively. Independent of the considered discretization, the opening of cracks starts at the head bolt. Subsequently, additional cracks start to grow in the vicinity of the support. If the loading is further increased, these micro-cracks coalesce with each other and form a macro-crack. This macro-crack results in a global softening behavior limiting the maximum loading. As expected, a better resolution of the localized failure mechanism is obtained from the fine mesh. For the coarse, the fracture zone is smeared over a larger domain. The shape of the zone, however, is only marginally affected by the mode of discretization.

6 CONCLUSION

A traction separation law has been developed, which takes permanent plastic deformations as well as anisotropic stiffness degradation into account. This interface law was derived by projecting a stress-strain relation onto a surface. For a simple calibration of the model, the softening evolution was determined by means of the fracture energy of the material. Since the considered additive decomposition of the displacement field holds in an incompatible sense, the displacement discontinuities and consequently, the traction separation laws are restricted to the material point level.

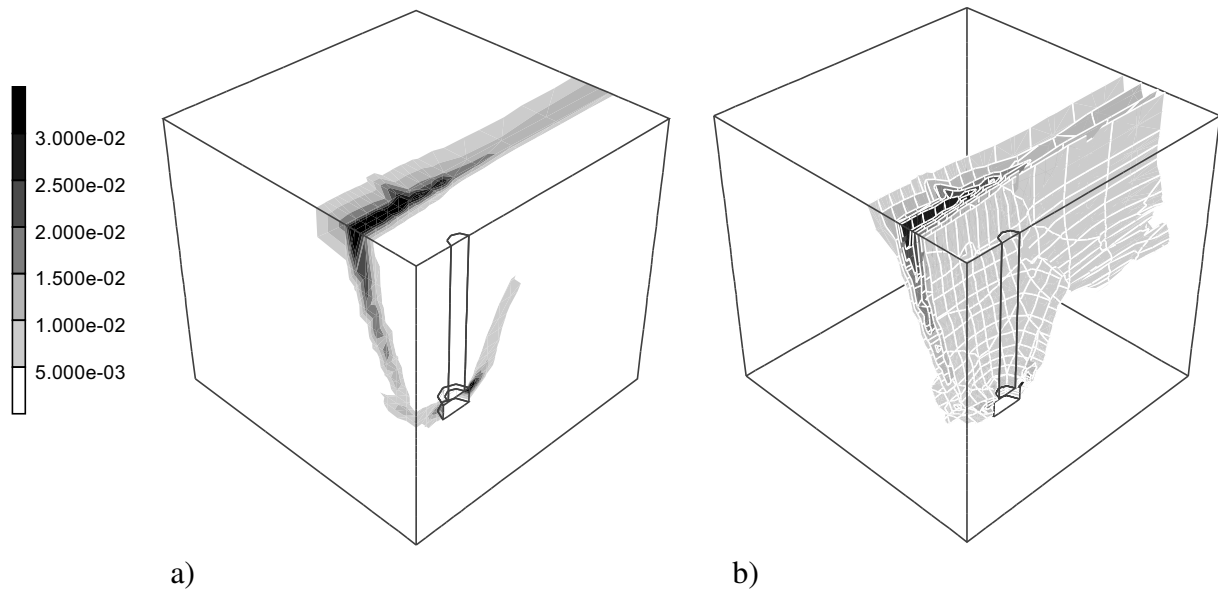


Figure 10: 3D finite element analysis of an anchor subjected to tensile loading (fine mesh): Distribution of the internal variable α representing the crack-width at $u_1 = 2.58 \cdot 10^{-2}$ cm: a) Contours along the surfaces, b) iso-surfaces.

The suggested traction separation law has been implemented into a finite element formulation. For the investigation of the applicability of the proposed finite element implementation, a two-dimensional academic benchmark problem (L-shaped slab) as well as a three-dimensional pull-out test of a steel anchor embedded in a concrete block are analyzed numerically. The analysis of the L-shaped slab demonstrated that both plastic strains as well as damage-induced stiffness degradation are captured. The robustness of the suggested implementation was documented by the analysis of the anchor pull-out test. Since the proposed integration algorithm of the constitutive laws is restricted to the material point level and formally identical to standard computational plasticity, any computer code for plasticity models can directly be used as the framework for the implementation.

References

- [1] R. De Borst. Some recent issues in computational mechanics. *International Journal for Numerical Methods in Engineering*, 52:63–95, 2001.
- [2] G. Pijaudier-Cabot and Z.P. Bažant. Nonlocal damage theory. *Journal of Engineering Mechanics (ASCE)*, 113:1512–1533, 1987.
- [3] Z.P. Bažant and G. Pijaudier-Cabot. Nonlocal damage, localization, instability and convergence. *Journal of Applied Mechanics*, 55:287–293, 1988.
- [4] H.B. Mühlhaus and E.C. Aifantis. A variational principle for gradient plasticity. *International Journal for Solids and Structures*, 28:845–857, 1991.
- [5] R. De Borst and H.B. Mühlhaus. Gradient-dependent plasticity: Formulation and algorithmic aspects. *International Journal for Numerical Methods in Engineering*, 35:521–539, 1992.

-
- [6] R. De Borst. Simulation of strain localization: A reappraisal of the cosserat continuum. *Engineering Computations*, 8:317–332, 1991.
- [7] P. Steinmann and K.J. Willam. Localization within the framework of micropolar elasto-plasticity. In V. Mannl, J. Najar, and O. Brüller, editors, *Advances in continuum mechanics*, pages 296–313. Springer, Berlin-Heidelberg, 1991.
- [8] J. Simo, J. Oliver, and F. Armero. An analysis of strong discontinuities induced by strain softening in rate-independent inelastic solids. *Computational Mechanics*, 12:277–296, 1993.
- [9] J. Simo and J. Oliver. A new approach to the analysis and simulation of strain softening in solids. In Z.P. Bažant, Z. Bittnar, M. Jirásek, and J. Mazars, editors, *Fracture and Damage in Quasibrittle Structures*, pages 25–39. E. &F.N. Spon, London, 1994.
- [10] J. Oliver and J. Simo. Modelling strong discontinuities in solid mechanics by means of strain softening constitutive equations. In H. Mang, N. Bićanić, and R. de Borst, editors, *Computational Modelling of concrete structures*, pages 363–372. Pineridge press, 1994.
- [11] J. Mosler and G. Meschke. 3D modeling of strong discontinuities in elastoplastic solids: Fixed and rotating localization formulations. *International Journal for Numerical Methods in Engineering*, 57:1553–1576, 2003.
- [12] J. Mosler. *Finite Elemente mit sprungstetigen Abbildungen des Verschiebungsfeldes für numerische Analysen lokalisierter Versagenszustände in Tragwerken*. PhD thesis, Ruhr Universität Bochum, 2002.
- [13] J. Oliver. Modelling strong discontinuities in solid mechanics via strain softening constitutive equations part 1: Fundamentals. part 2: Numerical simulations. *International Journal for Numerical Methods in Engineering*, 39:3575–3623, 1996.
- [14] F. Armero and K. Garikipati. An analysis of strong discontinuities in multiplicative finite strain plasticity and their relation with the numerical simulation of strain localization in solids. *International Journal for Solids and Structures*, 33:2863–2885, 1996.
- [15] A.R. Regueiro and R.I. Borja. A finite element method of localized deformation in frictional materials taking a strong discontinuity approach. *Finite Elements in Analysis and Design*, 33:283–315, 1999.
- [16] M. Klisinski, K. Runesson, and S. Sture. Finite element with inner softening band. *Journal of Engineering Mechanics (ASCE)*, 117(3):575–587, 1991.
- [17] T. Olofsson, M. Klisinski, and P. Nedar. Inner softening bands: A new approach to localization in finite elements. In H. Mang, N. Bićanić, and R. de Borst, editors, *Computational Modelling of Concrete Struct.*, pages 373–382. Pineridge press, 1994.
- [18] U. Ohlsson and T. Olofsson. Mixed-mode fracture and anchor bolts in concrete: Analysis with inner softening bands. *Journal of Engineering Mechanics (ASCE)*, 123:1027–1033, 1997.
- [19] F. Armero and K. Garikipati. Recent advances in the analysis and numerical simulation of strain localization in inelastic solids. In D.R.J. Owen, E. Oñate, and E. Hinton, editors, *Proc., 4th Int. Conf. Computational Plasticity*, volume 1, pages 547–561, 1995.

-
- [20] F. Armero. Localized anisotropic damage of brittle materials. In D.R.J. Owen, E. Oñate, and E. Hinton, editors, *Computational Plasticity*, volume 1, pages 635–640, 1997.
- [21] G. Meschke, R. Lackner, and H.A. Mang. An anisotropic elastoplastic-damage model for plain concrete. *International Journal for Numerical Methods in Engineering*, 42:703–727, 1998.
- [22] J. Simo and T.J.R. Hughes. *Computational inelasticity*. Springer, New York, 1998.
- [23] J.C. Simo. Numerical analysis of classical plasticity. In P.G. Ciarlet and J.J. Lions, editors, *Handbook for numerical analysis*, volume IV. Elsevier, Amsterdam, 1998.
- [24] J. Oliver. Continuum modelling of strong discontinuities in solid mechanics using damage models. *Computational Mechanics*, 17(1-2):49–61, 12 1995.
- [25] K. Garikipati. *On strong discontinuities in inelastic solids and their numerical simulation*. PhD thesis, Stanford University, 1996.
- [26] A.H. Berends, L.J. Sluys, and R. de Borst. Discontinuous modelling of mode-I failure. In D.R.J. Owen, E. Oñate, and E. Hinton, editors, *Computational Plasticity*, volume 1, pages 751–758, 1997.
- [27] R. Larsson, P. Steinmann, and K. Runesson. Finite element embedded localization band for finite strain plasticity based on a regularized strong discontinuity. *Mechanics of Cohesive-Frictional Materials*, 4:171–194, 1998.
- [28] M. Jirásek. Embedded crack models for concrete fracture. In R. de Borst, N. Bićanić, H. Mang, and G. Meschke, editors, *Computational Modelling of Concrete Structures, EURO C-98*, volume 1, pages 291–300, 1998.
- [29] N. Moës, J. Dolbow, and T. Belytschko. A finite element method for crack growth without remeshing. *International Journal for Numerical Methods in Engineering*, 46:131–150, 1999.
- [30] J. Dolbow, N. Moës, and T. Belytschko. An extended finite element method for modeling crack growth with frictional contact. *Computer Methods in Applied Mechanics and Engineering*, submitted, 2002.
- [31] I. Stakgold. *Green's functions and boundary value problems*. Wiley, 1998.
- [32] R.I. Borja. A finite element model for strain localization analysis of strongly discontinuous fields based on standard galerkin approximation. *Computer Methods in Applied Mechanics and Engineering*, 190:1529–1549, 2000.
- [33] P. Steinmann, R. Larsson, and K. Runesson. On the localization properties of multiplicative hyperelasto-plastic continua with strong discontinuities. *International Journal for Solids and Structures*, 34:969–990, 1997.
- [34] J. Hadamard. *Leçons sur la Propagation des Ondes*. Librairie Scientifique A. Hermann et Fils, Paris, 1903.
- [35] J. Oliver, A.E. Huespe, M.D.G. Pulido, and E. Samaniego. On the strong discontinuity approach in finite deformation settings. *International Journal for Numerical Methods in Engineering*, 56:1051–1082, 2003.

- [36] S. Govindjee, G.J. Kay, and J.C. Simo. Anisotropic modeling and numerical simulation of brittle damage in concrete. *International Journal for Numerical Methods in Engineering*, 38, 1995.
- [37] I. Stakgold. *Boundary value problems of mathematical physics*, volume I. Macmillien Series in Advanced Mathematics and theoretical physics, 1967.
- [38] I. Stakgold. *Boundary value problems of mathematical physics*, volume II. Macmillien Series in Advanced Mathematics and theoretical physics, 1967.
- [39] J. Mosler and G. Meschke. 3D FE analysis of cracks by means of the strong discontinuity approach. In E. Oñate, G. Bugada, and B. Suárez, editors, *European Congress on Computational Methods in Applied Sciences and Engineering*, 2000.
- [40] J. Mosler and G. Meschke. Embedded crack vs. smeared crack models: A comparison of elementwise discontinuous approaches with emphasis on mesh bias. *Computer Methods in Applied Mechanics and Engineering*, 2003. submitted.
- [41] M. Jirásek. Conditions of uniqueness for finite elements with embedded cracks. In E. Oñate, G. Bugada, and B. Suárez, editors, *European Congress on Computational Methods in Applied Sciences and Engineering*, 2000.
- [42] R. Lackner. *Adaptive finite element analysis of reinforced concrete plates and shells*. PhD thesis, Institut für Festigkeitslehre, Technische Universität Wien, 1999.
- [43] B. Winkler and G. Hofstetter. Experimental and numerical investigations of cracking of plain and reinforced concrete. In *International PhD Symposium in Civil Engineering, Vienna, Austria*, volume 1, pages 97–106, 2000.
- [44] J. Mosler and G. Meschke. Analysis of mode I failure in brittle materials using the strong discontinuity approach with higher order elements. In 2. *European Congress on Computational Mechanics*, 2001.
- [45] J. Hofman, R. Eligehausen, and J. Ožbolt. Behaviour and design of fastenings with headed anchors at the edge under tension and shear load. In R. De Borst, J. Mazars, G. Pijaudier-Cabot, and J.G.M. Van Mier, editors, *FRActure Mechanics of CONcrete Structures IV*, volume 2, pages 941–947, 2001.